Proc. SPIE Vol. 5894, p. 1-13, Advanced Wavefront Control: Methods, Devices, and Applications III; Mark T. Gruneisen, John D. Gonglewski, Michael K. Giles; Eds., Aug 2005

Development of an Adaptive Optics Test-Bed for Relay Mirror Applications

Justin D. Mansell†[2], Arturo A. Jacobs[1], and Morris Maynard[2]

[1]*Boeing-SVS, Inc.*
[2]*MZA Associates Corporation*

ABSTRACT

The relay mirror concept involves deploying a passive optical station at a high altitude for relaying a beam from a laser weapon to a target. Relay mirrors have been proposed as a method of increasing the range of laser weapons that is less costly than deploying a larger number of laser weapons. Relay mirrors will only be effective if the beam spreading and beam quality degradation induced by atmospheric aberrations and thermal blooming can be mitigated. In this paper we present the first phase of a multi-year effort to develop a theoretical and experimental capability at Boeing-SVS to study these problems. A team from MZA and Boeing-SVS has developed a laboratory test-bed consisting of a distributed atmospheric path simulated by three liquid crystal phase screens, a Shack-Hartmann wavefront sensor, and a MEMS membrane deformable mirror. We present results of AO component calibration and evaluation, the system construction, and the system performance.

1. Introduction

One concept for extending the range of laser weapons is the use of relay mirrors.[1] There are many different proposed designs, but in general a relay mirror is an optical system that is stationed at a high altitude and redirects light from a high energy laser (HEL) source to a target. The relay mirror concept has been under development for many years. A large-scale demonstration lead by Ball Aerospace was completed in the early 1990's in which a laser was reflected from an orbiting satellite relay mirror and relayed to a target on earth.[2] Today, the Aerospace Relay Mirror System (ARMS), currently undergoing system testing at Boeing-SVS, is planning on doing a similar experiment using a high-altitude airship as the relay mirror platform.[3]

Some proposed relay mirror system designs include adaptive optics (AO) systems with varying complexity. Relay mirror adaptive optics systems are typically different than those studied for other applications like astronomy and single-platform laser weapons in several key ways. In the relay mirror case, a cooperative beacon can be placed on the relay to allow for accurate sampling of the wavefront distortions by the source. Since this beacon can be coherent, wavefront sensing can be done with self-referencing interferometers (SRIs) instead of the traditional Hartmann sensor. AO systems can be placed on the source or on the relay or on both ends of the engagement. The AO systems can have varying complexity and can include multiple deformable mirrors for both wavefront and intensity profile control.

The goal of this work is to explore and demonstrate possible AO systems for relay mirror applications. This project began by studying the relay mirror problem with WaveTrain, a commercial physics, controls, and wave-optics code developed by MZA Associates Corporation over the last two decades that is free for use on any government-funded project.[4] After several years of studying the problem, construction began on an adaptive optics test-bed for evaluating various AO concepts for relay mirrors. In this first year, a basic AO system was designed, built, and evaluated. This paper describes the results of some relay mirror modeling and the development and demonstration of the AO test-bed.

2. Modeling

2.1. Basic Relay Engagement Modeling

The two physical effects that are the primary causes of relay system performance degradation are diffraction-induced decoupling from the relay receiver telescope and beam quality degradation due to atmospheric turbulence. To

† *jmansell@mza.com*

determine the magnitudes of each of these effects, a basic relay system made up of two telescopes was modeled while varying the separation distances. The propagation between the source and receiver apertures was modeled with no atmospheric turbulence and with a Clear 1 atmospheric turbulence model.[5] The source and receiver were modeled at 12-km and 23-km altitudes respectively. Each data point is the result of averaging 100 random realizations of the atmosphere. The model used a wavelength of 1315 nm. The model was run for propagation with and without turbulence to separate the effects of diffraction and atmospheric distortion. In all cases the source and receiver aperture diameters were both 1.5 m. The model was also run with and without the receiver aperture central obscuration (CO) to separate the effects of the telescope aperture shape. The central obscuration was 0.5-m in diameter on the source and was the same size on the receiver, when it was used. Figure 1 shows the WaveTrain model. The four cases of propagation with and without atmospheric distortion and with and without a central obscuration in the receiver telescope were modeled simultaneously for computational efficiency.

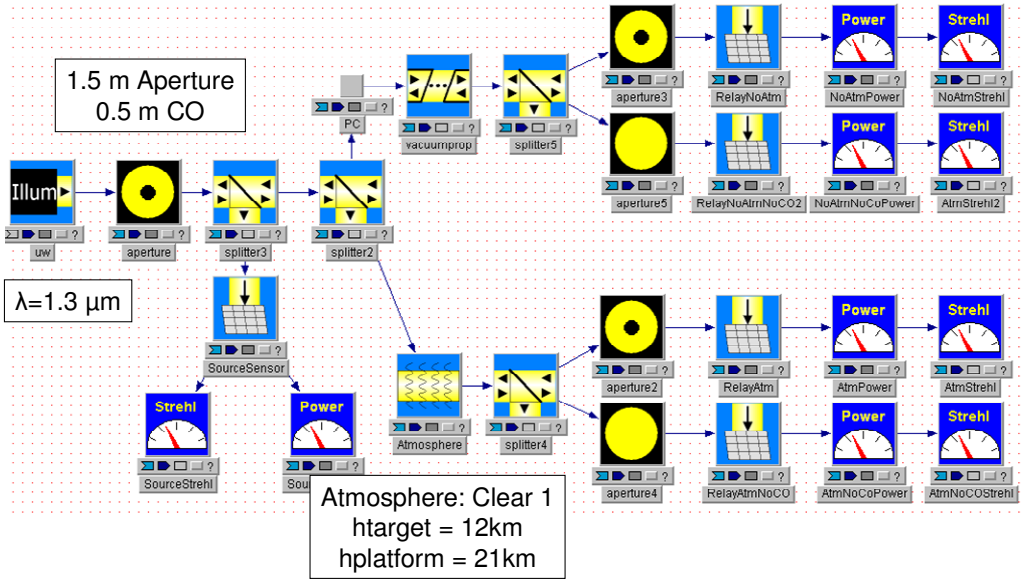

Figure 1 - WaveTrain model of the simple relay engagement

Figure 2 shows the normalized received power (NRP) of the relay engagement with respect to propagation distance and the difference in the NRP with and without the central obscuration for the case of no atmosphere and with the atmospheric model. The NRP is the ratio of the power received by the relay telescope to the power launched by the source. The deleterious effect of the atmosphere can be clearly seen by comparing the results with and without atmospheric-induced distortion.

These results also show the effect of the central obscuration on the system performance. In the case of vacuum propagation (no atmosphere) and no receiver CO, the NRP loss is due to the diffractive spreading of the beam beyond the receiver aperture. The presence of the receiver CO results in additional power loss due to diffraction of the light into the center of the

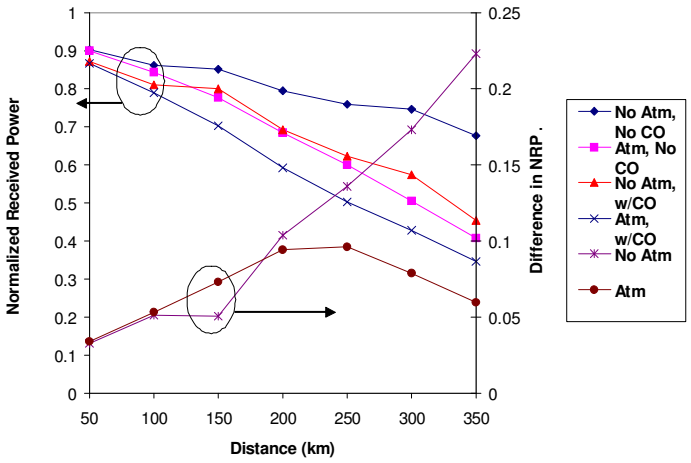

Figure 2 - Normalized received power for a simple relay engagement modeling

beam. The difference between the NRP between the two cases without atmospheric turbulence shows that the CO consistently degrades the NRP as the propagation distance increases. This does not appear to be the case when the atmospheric distortions are included in the model. The difference between the two cases with atmospheric distortions shows that the reduction in NRP due to the CO is largest at a 250-km propagation distance, but it decreases as the range is increased beyond that point.

Figure 3 shows the phase-removed Strehl ratio with respect to propagation distance for a receiver telescope with and without a central obscuration. The phase-removed Strehl ratio is calculated by removing the phase of the input electric field and comparing the amplitude of the phase-removed far-field diffraction spot with that of the electric field that is not phase-removed. It is clear that the presence of the central obscuration has little effect on the Strehl ratio. It is also clear that even for short engagements, the beam quality is substantially reduced by the propagation through the atmosphere. This reduction in Strehl ratio is a much more significant effect than the reduction in NRP.

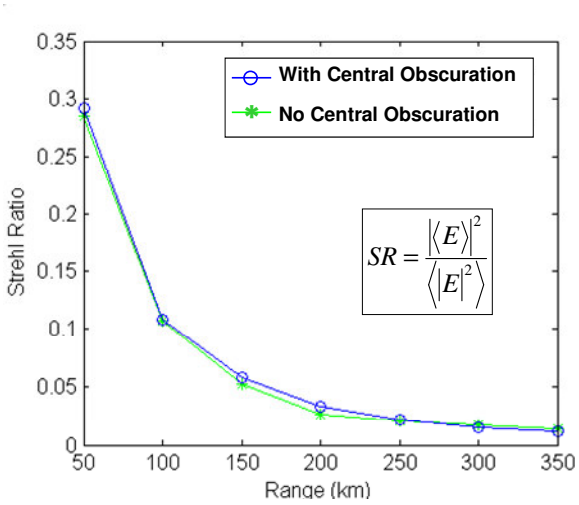

Figure 3 - Strehl ratio for modeling a simple relay engagement

2.2. Relay Modeling with Various Adaptive Optics Configurations

Propagation of laser beams through the atmosphere with different adaptive optics configurations has been extensively studied.[6,7] Boeing-SVS has been involved in wave-optics simulations of relay engagements over the last several years. Many different configurations have been explored, including using single and multiple deformable mirrors, using different types of wavefront sensors, and using different types of control algorithms. The details of this analysis is outside the scope of this paper, but this modeling shows that the adaptive optics systems cause both the beam quality and the capture efficiency can be increased, although the effect of the beam quality increase was much more significant to the overall system performance. The success of application of AO to the relay mirror system performance in modeling warranted further study of AO system for relay mirrors at the laboratory scale.

3. Laboratory Component Evaluation and Description

Laboratory-scale demonstrations were conceived to confirm this modeling and to demonstrate the efficacy of AO for relay mirror engagements. The system was designed with conventional optics and three key commercial off-the-shelf (COTS) components: a liquid crystal spatial light modulator, a Shack-Hartmann wavefront sensor, and a MEMS membrane deformable mirror. The three key components were purchased for other projects at Boeing-SVS, not for the AO demonstration, so they did not exactly match the ideal specifications for an AO system, which presented several challenges in creating an AO system with these components that will be addressed later in this paper. Before constructing an AO system with these components, each of them needed to be tested and characterized.

3.1. Liquid Crystal Phase Modulator

A Boulder Nonlinear Systems (BNS) liquid crystal spatial light modulator (LC SLM) was chosen to impose atmospheric phase screens on the beam. The square array of LC phase modulators has 512 pixels on a side with 15 micron pitch. The temporal response of the LC was measured by reflecting a beam from the LC onto a photodiode and switching on and off a diffraction grating pattern. Rise and fall times were measured to be 50 and 75 ms respectively. Based on this measurement, the LC has the slowest response of all the devices in the setup.

3.1.1. Calibration of the Voltage-to-Phase Response

Before the SLM could be introduced into the adaptive optics experimental setup, the voltage-to-phase response needed to be measured and the static aberrations needed to be removed. The DAC on the LC SLM is linear, but the response of the LC to voltage is nonlinear. Therefore a relationship between the voltage and phase had to be determined to make

effective use of the LC SLM in the laboratory. A first calibration attempt was made using an interferogram of the LC SLM. A Michelson interferometer was built to calibrate the voltage response. The image of the LC was placed onto a CCD using a singlet imaging lens. A large tilt was put onto the reference mirror to create a set of fringes on a CCD. The top half of the LC was not modulated, but the lower half was given a piston phase shift by writing a fixed voltage to all the pixels. Figure 4 shows a typical image with a phase shift applied. The piston phase shift causes the fringes in the lower half to move relative to the upper half. The amount of motion is directly proportional to the phase shift. The intensity ratio above and below the LC SLM is also related to the phase shift.

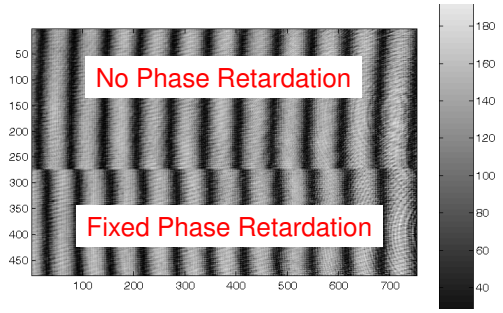

Figure 4 - Phase shift on the LC SLM.

The initial calibration was done using the intensity on the CCD directly above and below the phase shift. Five lines of the CCD above and below the phase discontinuity were averaged to minimize noise effects. An intensity maximum near the middle of the SLM image was used to isolate a column for analysis. The ratio of the intensity measured above the phase discontinuity, which was an intensity peak, to the intensity measured below the phase discontinuity was used to find the phase shift via the equation,

$$\Delta\phi = \cos^{-1}\left(\sqrt{\frac{I_{measured}}{I_{\max}}}\right)$$

where I_{max} is the maximum intensity of the unmodulated fringe pattern and $I_{measured}$ is the intensity measured on the half with the phase shift. Several calibration runs were made using the intensity ratio technique, but all the results showed a very jagged and noisy response curve due to noise in the measurement system. To minimize this effect, another method of phase calibration was devised to minimize the effects of this noise.

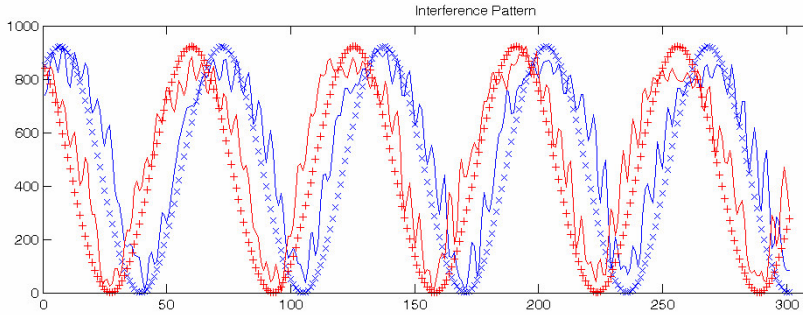

Figure 6 - Measured interferometer fringes above and below the phase discintinuity induced by the LC SLM and their corresponding fits.

A common technique for mitigating systematic noise is to fit the measurement to a theoretical curve. Since a sinusoidal curve along one axis of the image was predicted by theory due to the large tilt imposed in the reference arm of the interferometer, we fit the average of 5 rows of the CCD measurement to a cosine curve both above and below the phase discontinuity induced by the LC SLM. The upper un-shifted interferometer fringes were first fit with both the frequency and the phase as free parameters. Then the lower shifted fringes were fit using the frequency result of the first fit and having only phase offset as a free parameter. Figure 5 shows

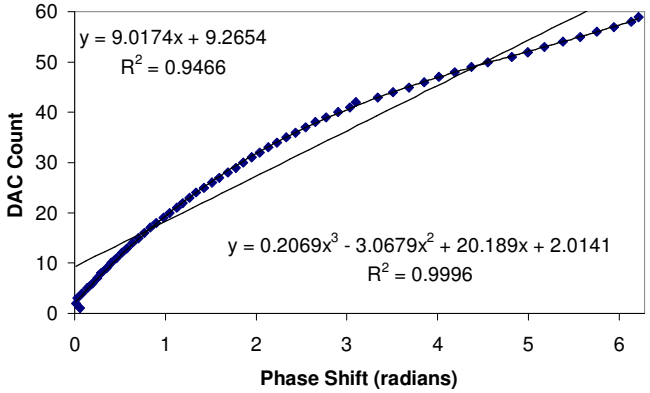

Figure 5 - Relationship between phase shift and DAC output.

an example measurement of the fringes for a given DAC voltage. The difference between the phases of the two fit results is equal to the measured phase shift due to the LC SLM. Note that if the fringes are not exactly vertical due to wavefront tilt in the orthogonal axis, an additional constant phase shift term is seen as well, but it can be subtracted from all measurements since the zero-voltage case should have zero phase shift. This technique was applied over all the DAC outputs and the result was used to determine the relationship between phase shift and DAC voltage shown in Figure 6. This relationship is often implemented as a look-up table (LUT), but we found that the smooth nature of the curve lent itself to a 3rd order polynomial fit, as shown in Figure 6.

3.1.2. Backplane Aberration Compensation

The LC SLM devices typically have some static aberration on them, usually attributed to the warp in the silicon backplane. In order to use the LC SLM to impose only the desired spatial phase, the static aberrations on the LC needed to be determined and compensated. The LC was initially taken to a commercial Zygo interferometer to measure the aberrations. The aberrations were decomposed into Zernike terms by the Zygo software. Then the LC SLM was returned to the laboratory Michelson interferometer. The phase screen composed of the Zernike terms measured by the Zygo interferometer was then imposed on the LC and the static aberrations were greatly reduced. Figure 7 shows the resulting interference pattern. The unit radius of the Zernike terms was the corner of the LC, not the edge so that the higher powered radial terms did not unnecessarily warp the corners of the LC.

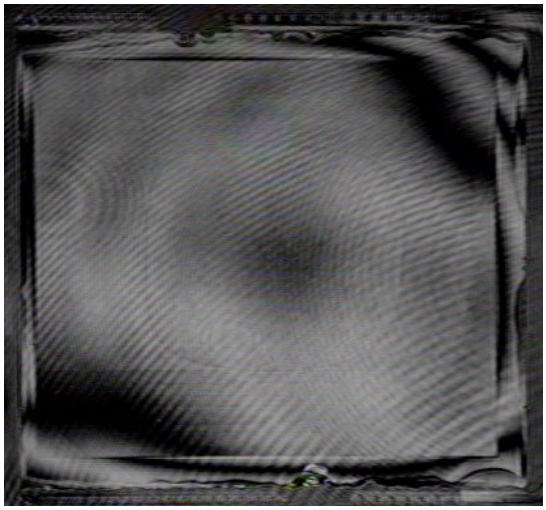

Figure 7 - Initial Zygo static aberration field.

This Zygo-determined compensation phase screen was used for the single phase screen adaptive optics experiments, but was found to be insufficient for the triple-pass. In the triple-pass configuration, the beam was sufficiently distorted by the liquid crystal relative to that when replaced by an optical flat to justify reinvestigating the static aberration compensation screen.

We decided to try to fine-tune the LC SLM compensation by creating a program to automatically search through the Zernike coefficients, but some form of feedback metric was needed to determine the search efficacy. To find such a metric, the LC SLM was returned to the laboratory Michelson and a large diagonal tilt was placed on the reference arm. The fringes were fairly straight and parallel with the original static aberration compensation, but did have some curvature that indicated some residual aberration. The fringe curvature inspired a method for optimizing the LC backplane compensation.

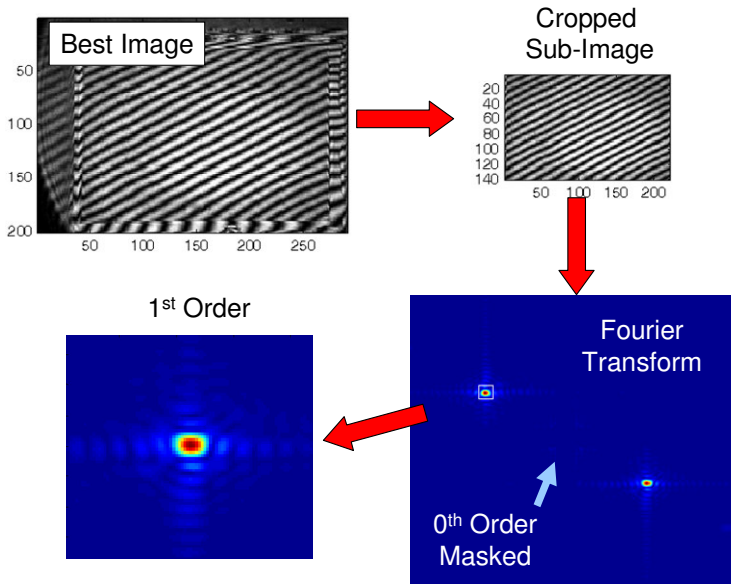

Figure 8 - Analysis procedure for feedback on the LC compensation.

Figure 8 illustrates the procedure

used for obtaining a feedback metric. The fringe pattern over the active area of the LC SLM that was imaged onto the CCD was digitally Fourier transformed using the fast Fourier transform (fft) algorithm. If the fringes were perfectly straight, the Fourier transform would show a two-dimensional sinc pattern in the first orders of the Fourier transform. Instead highly aberrated digitally "diffracted" orders were apparent. A search was performed over the coefficients of the lowest 33 Zernike polynomials using the sum of the x and y second moments of the +1 diffracted order as a feedback metric. After a short search, the phase screen was sufficient to remove the beam distortions in the triple pass configuration. Figure 9 shows the resulting interferogram. It is possible that moving the CCD to the focus of the imaging lens would have eliminated the need for a digital Fourier transform. In retrospect, it would have been fairly straightforward to implement four-bin interferometry once a good phase to voltage relationship had been established by using the LC SLM as a phase shifter.

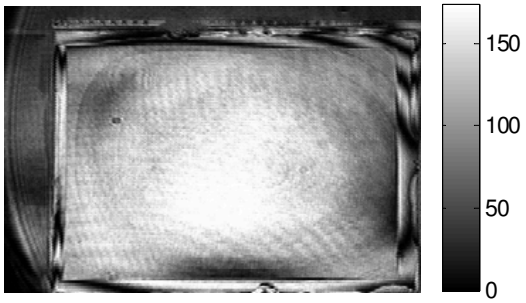

Figure 9 - Interferometer image after optimizing the digitally diffracted orders of the tilted interference pattern.

WaveTrain was used to generate a set of Kolmogorov phase screens and the point-spread function (PSF) of an aberrated circular uniform-intensity beam. The same phase screens were written to the LC SLM and the beam PSF was measured on a CCD. Figure 10 shows two such PSFs from the simulation and the laboratory. A visual comparison of the measurements showed that they matched well.

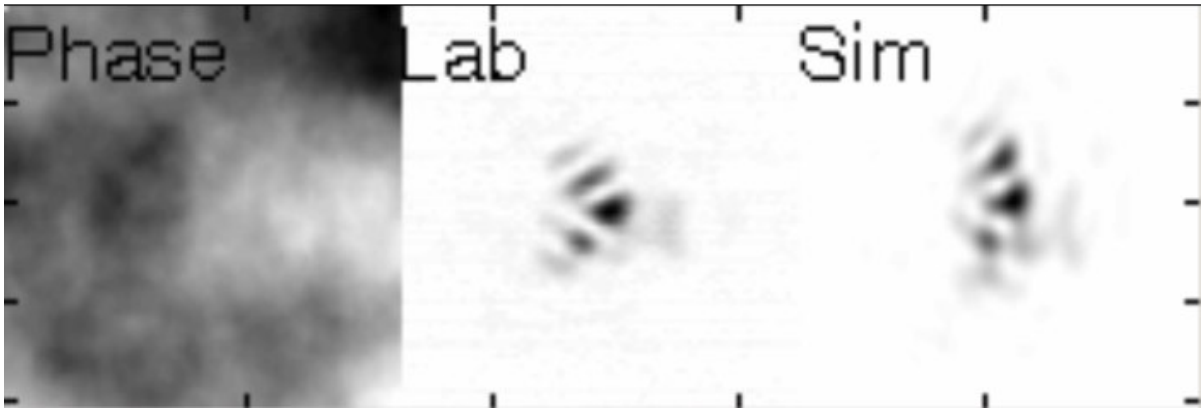

Figure 10 – An example written phase screen and a comparison of PSF induced by the LC SLM in the lab with the PSF determined using a WaveTrain simulation.

3.2. Wavefront Sensor

The Shack-Hartmann Wavefront Sensor (SHWFS) provided for this experimental setup was manufactured by Wavefront Sciences. The SHWFS was composed of a 10-bit Cohu camera and a 2-mm focal length lens array. The square lenses in the array are 72-microns on a side. When this SHWFS is fully illuminated, there are more than 5500 lenses visible on the CCD. This SHWFS was designed to have a large spatial resolution at the expense of phase tilt resolution.

WaveTrain software was used to reduce the SHWFS image into slopes and into a wavefront surface using a Southwell reconstruction algorithm. To test the software, a 250-mm focal length lens was measured in differential mode.

The rms wavefront slope noise floor was determined by creating a calibration file in the laboratory and then analyzing a series of 20 WFS images relative to the initial calibration frame. The average rms wavefront slope was measured to be 257 and 200 μradians for x and y respectively. After a Southwell reconstruction, the rms wavefront error was 273 nm.

To verify the alignment and imaging between the SLM and the WFS, atmospheric aberrations were written to the LC and read on the WFS. Figure 11 shows one such comparison. In all cases, the measured and written phase screens matched well. The average RMS difference between the measured and written phase screens 673 nm. Most of the large magnitude phase errors were found at the edges of the phase screens and were attributed to slight registration and scaling errors between the measured and written screens.

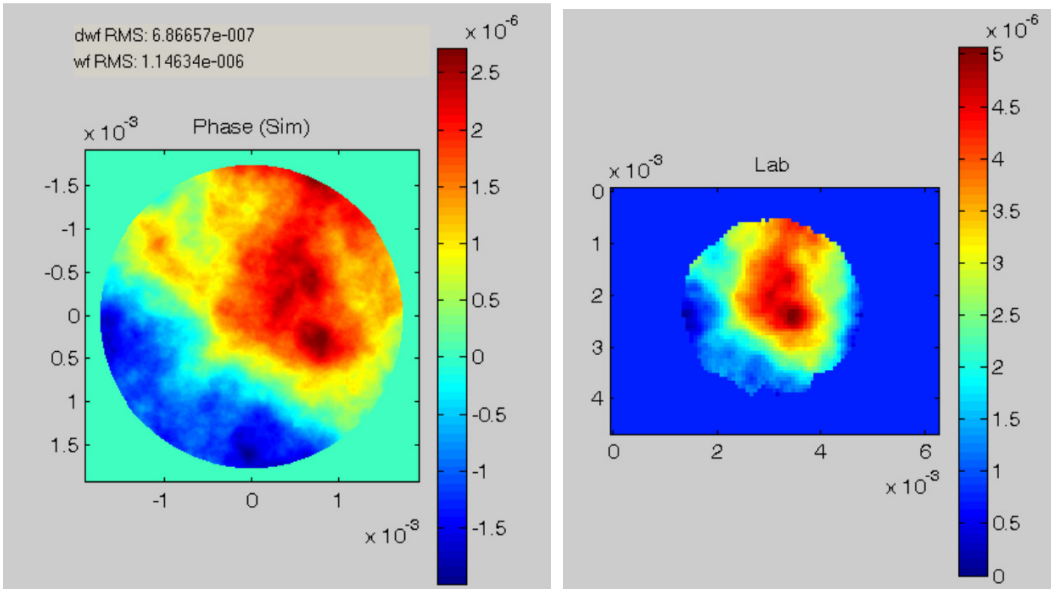

(a) (b)

Figure 11 - Comparison of the phase screen written to the LC, (a), with that measured by the Shack-Hartmann wavefront sensor, (b).

3.3. Deformable Mirror

The deformable mirrors (DMs) provided for this project were manufactured by AgilOptics. The 25-mm diameter DM has 37 electrostatic actuators. The mirror membrane was coated with aluminum for reflectivity.

The surface figure of each of the two deformable mirrors available for this project was evaluated. The first mirror had static aberrations of 300 nm magnitude peak-to-valley. A Zernike fit to the mirror aberrations showed that the aberrations were primarily astigmatism. The second mirror was substantially flatter with an rms wavefront error of only 65 nm rms.

3.3.1. Characterization of Influence Functions

The DM actuators were modeled by solving the equation,

$$\nabla^2 z = \frac{F}{T}$$

using finite element analysis in Matlab. In this equation, F represents the force on the membrane surface and T represents the mirror tension. The electrostatic force was calculated using the equation,

$$F = \frac{\varepsilon \cdot A \cdot V^2}{2 \cdot d^2} \ ,$$

where ε is the permittivity, A is the actuator area, V is the applied voltage, and d is the separation between the mirror membrane and the electrostatic pad.

Each of the influence functions was measured in the lab. The central influence function shape was compared to the theoretical shape predicted by the Matlab simulation. Figure 12 shows the cross-sections of the mirror's central influence function measured in the laboratory with the Shack-Hartmann wavefront sensor and predicted by the model. The modeled influence functions accurately predicted the laboratory mirror performance.

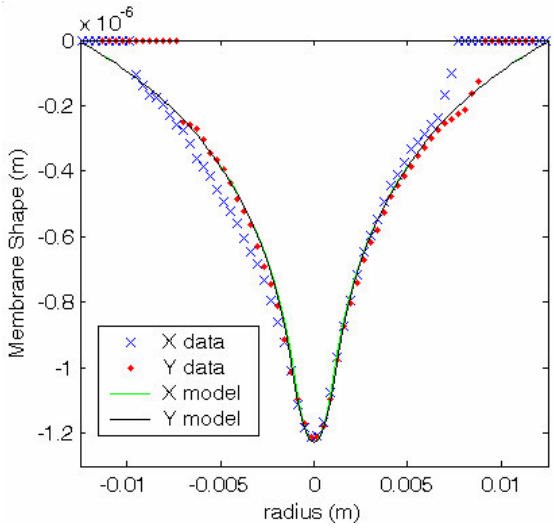

Figure 12 - Measured and theoretical central influence function.

The mirror surface was measured with the SHWFS as the mirror was biased in steps up to 60 V. The rms wavefront deformation was fit to the expected parabolic voltage dependence. The maximum rms mirror deformation in this experiment was 350 nm. The rms fit error was 5 nm.

During experimentation with the first mirror, an accidental over-voltage condition caused the mirror to rupture due to electrostatic snap-down. After this incident, force limiting software was added to the device driver that interfaced the computer to the DM drive electronics. This software calculated the average effective voltage on the DM and would not allow the user to exceed this voltage. The formula for this calculation was

$$V_{eff} = \sqrt{\frac{\sum_{i=1}^{N} V_i^2}{N}},$$

where N is the number of actuators and V_i is the actuator voltage. This calculation would need to be modified to include the actuator area if the area of the actuators was not equal.

4. Software Setup and Methodology

To minimize duplicated development and maximize traceability to simulation, WaveTrain was chosen to both simulate the laboratory experiment and to serve as the core of the software control of the laboratory equipment. Figure 13 shows the WaveTrain system used to control the laboratory experiment. A single loop begins when a phase screen is generated by the Atmospheric Path (AtmoPath2). The phase screen is then interpolated to the liquid crystal pixel grid (a 256 square pixel array with 15-micron pitch representing one quadrant of the LC). Then the tilt is removed from the grid to avoid spending DM throw compensating for tilt and to avoid the complexity of a steering mirror. Then the static aberration compensation is added to the grid. Finally, the LUT block introduces the 2π phase resets and converts the phase screen from radians to DAC counts for export to the LC SLM.

After the phase screen is written to the LC SLM, an image is taken from the SHWFS and fed back into the WaveTrain system. WaveTrain then reduces the image into slopes, adds a focus term to the slopes, multiples the slope vector times the control matrix, and converts the DM forces into voltages and DAC commands. The focus addition was done in WaveTrain to compensate for the parabolic bias of the DM, which is explained later in this paper in more detail. This static bias could be compensated optically, but doing it digitally offered us more flexibility without having to significantly increase computational complexity or modify the optical setup.

Matlab was used as the backbone of the laboratory system to interface with the WaveTrain mex system and the hardware via dynamic linked library (DLL) calls. Future efforts will be to leverage the automatic code generation feature of WaveTrain to interface it directly with the hardware and use a second process to tap a shared memory buffer to display the results.

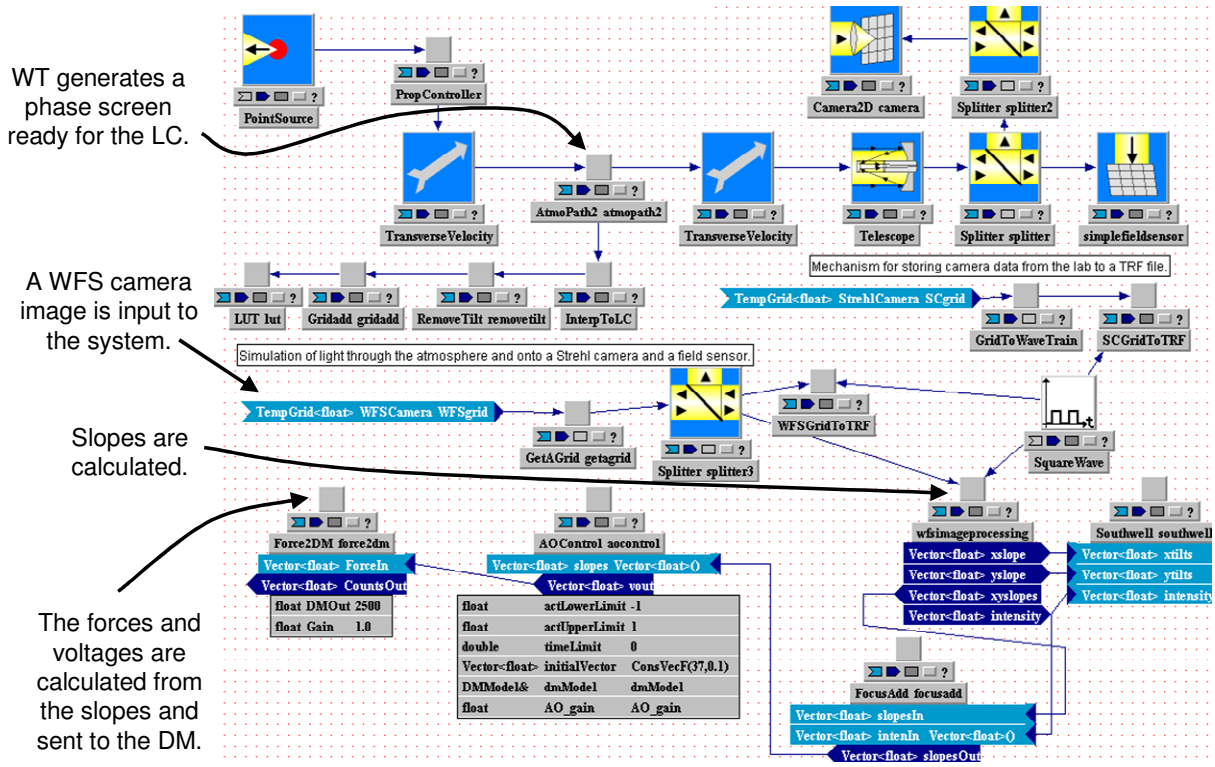

Figure 13 - The WaveTrain block diagram of the laboratory system.

5. Optical Design

After the devices were all characterized, they were assembled into a basic AO system designed to mimic the situation where there is no AO on the source side and only AO on the relay. Figure 14 shows the optical setup of the proposed system. Light from the laser is conditioned in polarization with a half wave plate (HWP) and a polarizing beam splitter (PBS). (Even though we were using a polarized laser, we found the PBS to be important to get good results from the LC SLM.) The Gaussian beam is then expanded by 20x and sent through a 1.75-mm diameter aperture, which creates the system pupil. This system pupil is imaged onto the LC SLM, onto the deformable mirror (DM), and onto the Shack-Hartmann wavefront sensor (WFS). After transmission through the aperture, the beam is fairly uniform in intensity. Then the beam is magnified by a 2x optical telescope formed by a 250-mm focal length and a 125-mm focal length lens pair. Then the beam bounces off of three quadrants of the LC SLM over a 650-mm path. The average phase tilt was removed from each of these phase screens to avoid the complexity of a steering mirror. This tilt removal also prevented the beam position on the liquid crystal from changing during the experiment, which prevented any misregistration. The Fresnel

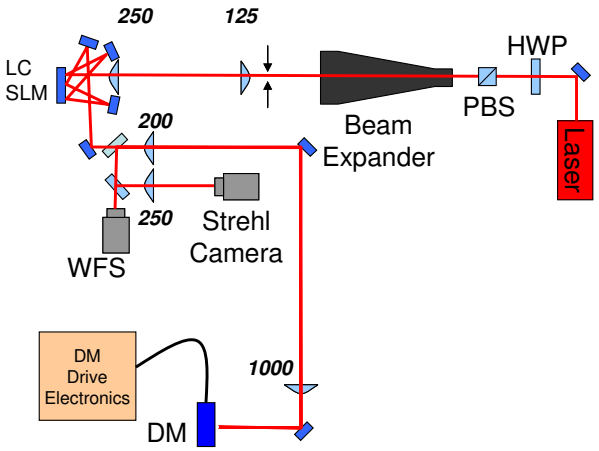

Figure 14 - Optical Setup

number for this propagation, which is given by $D^2/\lambda z$ (where D is the aperture diameter, λ is the optical wavelength, and z is the propagation distance), is 30.

Light from the LC SLM propagates over a 225-mm path to a telescope that expands the 3.5 mm beam to a 17.5 mm beam to illuminate the DM. This telescope is comprised of a 1000-mm focal length lens and a 200-mm focal length lens. After reflection from the DM, the light returns through the telescope to a beam splitter that reflects light into the WFS and onto a Strehl Camera.

6. System Characterization

6.1. Adaptive Optics with a Single Phase Screen

6.1.1. Control Matrix Generation

The first step in closing the adaptive optics loop is the generation of the control matrix. The normal procedure for generating this matrix is to create a poke matrix using the slopes of the influence functions measured from the SHWFS and then invert the poke matrix using singular value decomposition to generate a control matrix.[8] When the wavefront sensor and deformable mirror are well matched, there are about as many illuminated lenses as there are actuators on the deformable mirror. Due to budgetary and time constraints, the adaptive optics system described here was constructed with parts that were obtained for other purposes. The wavefront sensor was purchased for optical metrology. The deformable mirrors were purchased several years before the commencement of this project for potential future AO projects. Because this equipment was not designed for this AO development, the AO components were not well matched. The 5000+ lens Shack-Hartmann wavefront sensor was designed for high spatial resolution, but the deformable mirrors only have 37 actuators. This mismatch was studied before constructing the AO system.

There were several different possible techniques considered for handling the SHWFS and DM mismatch. One possible technique considered was to reduce the beam size to only illuminate a small number of lenses. This approach could not be use effectively in this experiment because the WFS measurement noise required averaging over a large number of slope measurements to be of reasonable accuracy. It was convenient in this optical setup to make the beam size on the SHWFS match the beam size on the LC SLM, which allowed approximately 1500 lenses to be illuminated. Two different techniques were evaluated to handle the large number of illuminated lenses. The standard technique of using the all the lenses and generating a large control matrix was employed. Another technique that was evaluated involved clustering the lenses into "super-lenses" by averaging the slope measurements over the lens cluster.

A computer simulation was setup in which a 37 actuator DM was controlled by a SHWFS with 885 illuminated lenses. In one case, these lenses were reduced into an array of 7x7 super-lenses for control. In another case, all 885 lenses were used for control. Fig 9 shows the mapping of the lens array into the 7x7 super-lenses. The control matrix was generated with no slope noise on the SHWFS, but during control, 100 µrads of slope noise was imposed on the slope measurements. The simulated aberration was a focus term since after tilt, second order terms are the most prominent term in the Kolmogorov turbulence distribution. In this simulation, control with the cluster of super-lenses converged to an average rms slope magnitude of 67.5 µrads and the full array control converged to an average rms slope

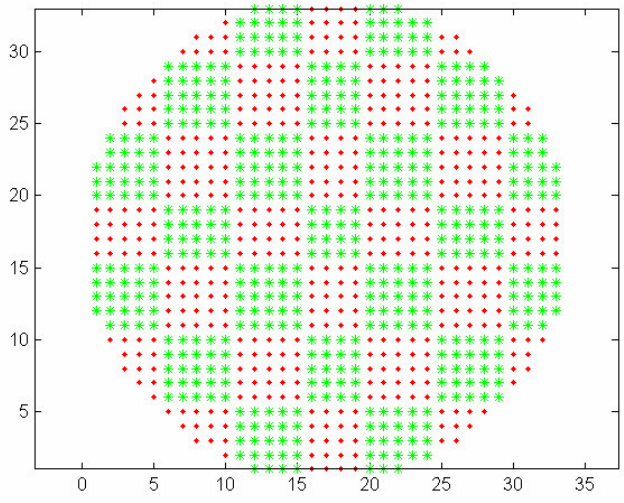

Figure 15 - Mapping of the clustering of the super-lenes. The asterisks and diamonds represent different lens clusters.

magnitude of 18.7 μrads.

Mathematical analysis of the super-lens clustering technique showed that using the larger number of lenses in the control matrix is equivalent to a weighted average of the slopes. A large control matrix was determined to be the best for this experimentation since the goal was to achieve the smallest wavefront error possible and the computational expense was negligible in the laboratory environment.

6.1.2. Digital Curvature Bias Subtraction

When biased to a central voltage, most conventional deformable mirrors move in piston. Membrane deformable mirrors take on a parabolic shape instead. The standard way of handling the curvature bias of membrane deformable mirrors is to adjust the imaging telescope between the DM and the SHWFS to result in a wavefront curvature incident on the DM which matches the curvature on the DM. This procedure works well if the bias is not going to be varied, but requires that at least one lens of the telescope and DM be on translation stages if it is going to be varied during experimentation.

To avoid having this extra hardware complexity, an alternative method of handling the curvature bias was employed. The telescope was setup to image the DM without adding or subtracting any curvature. Then the DM was put under bias and the curvature was measured on the SHWFS. That curvature was then subtracted from the slope measurements during closed loop operation. This technique adds to the computational complexity, but dramatically increases the system flexibility and reduces the hardware complexity. When an optimal bias is determined, the additional computational complexity can be taken out by recalibrating the SHWFS with the curvature on the DM.

The only hardware element that had to be adjusted as a result of changing the DM bias was the focus on the metric camera. Once the DM curvature bias was established, this focus could be locked down for all future experimentation.

6.1.3. Performance Characterization Metrics

Several different performance metrics were used to characterize the system results. Two metrics were based on the point spread function (PSF) measured with the independent CCD camera: Strehl ratio and Power in the Bucket (PIB). Both of these metrics were compared to the values obtained from the best PSF, which was measured in the lab with no aberration applied to the liquid crystal and the PSF was optimized with the DM using a genetic search algorithm. To get a visual determination of the performance enhancement, the PSF was averaged over multiple frames after being recentered to the first moment to show the performance enhancement as well.

6.1.4. Single Phase Screen Results

The adaptive optics control loop was closed for a variety of turbulence strengths. In each of the situations a Greenwood frequency of 70 Hz was used. Table 1 summarizes the closed loop results. All the results are for a 100-frame average.

Table 1 - Single Phase Screen Results

D/r_0	Closed Loop Strehl Ratio	Open Loop Strehl Ratio
3	89%	70%
5	76%	56%
7	73%	49%

Table 2 - Results for Varying Mode Removal

Number of Modes Removed	Strehl Ratio
1	69.3%
4	69.8%
16	71.8%
30	71.0%

Analysis was also done using various numbers of modes of the control matrix for a Greenwood frequency of 70 Hz and a D/r_0 of 7. In each case the average open-loop Strehl Ratio was 48.7%. Table 2 shows the results of this experimentation. It appears that the system performance is fairly insensitive to the number of modes removed from the control matrix. This is expected since the preponderance of aberrations in a Kolmogorov phase screen is in the low spatial frequency modes, which have the largest gains in the control matrix of a membrane mirror.

6.2. Adaptive Optics with a Distributed Phase Screen

After success with a single phase screen, multiple phase screens were written to the LC SLM to simulate a distributed atmosphere.

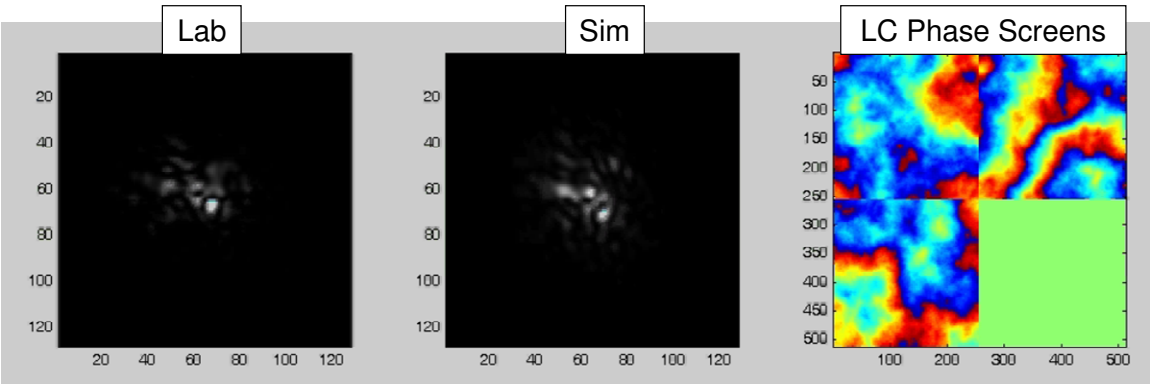

Figure 16 – Laboratory and simulation PSF after reflection from three LC phase screens.

The time-averaged PSF averaged over 50 frames in Figure 17 shows that the AO system is working. The Strehl ratio improved by a factor of 2.07. Work is continuing to tie these results to the modeling and continue the AO system characterization.

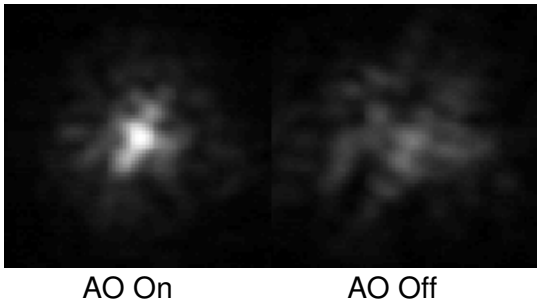

Figure 17 - Results of the closed loop operation with three phase screens each with $D/r_0 = 7$ and f_G=100 Hz.

7. Conclusions & Future Work

This paper describes the wavefront control problem faced by the relay mirror engagement and the first stage of development of an adaptive optics test-bed for studying relay mirror AO systems. Each of the components were tested and calibrated. The closed-loop AO system was successful at removing aberrations and increasing the system Strehl ratio. Future work on this project will involve continued anchoring the laboratory results of the system to the WaveTrain model, adding a counter-propagating beam to simulate a beacon/HEL scenario, adding a mechanism for adjusting the Fresnel Number, and exploration of more advanced AO concepts including multiple AO systems.

8. References

[1] E. A. Duff and D. Washburn. "The Magic of Relay Mirrors", Proc. SPIE, Vol. 5413, 137-144 (2000).

[2] J. S. Dierks, S. E. Ross, A. Brodsky, P. W. Kervin, and R. W. Holm. "Relay Mirror Experiment overview: a GBL pointing and tracking demonstration", Proc. SPIE, Vol. 1482, p. 146-158 (1991).

[3] G. Marsh. "Airships Return", Avionics Magazine (April 2004).

[4] www.mza.com

[5] Robert R. Beland, "Propagation Through Atmospheric Optical Turbulence" in the Infrared and Electro-Optical Handbook, Vol. 2, Joseph S. Accetta and David L. Schumaker, Editors, ERIM, Ann Arbor, MI and SPIE, Bellingham, WA, 1993.

[6] J. D. Barchers, D. L. Fried, and D. J. Link. "Evaluation of the performance of Hartmann sensors in strong scintillation" Applied Optics, Vol. 41, No. 6, p. 1012-21 (2002).

[7] J. D. Barchers, D. L. Fried, D. J. Link, G. A. Tyler, W. Moretti, T. J. Brennan, and R. Q. Fugate. "The performance of wavefront sensors in strong scintillation", Proc. SPIE, Vol. 4839, p. 217-27 (2003).

[8] C. Paterson, I. Munro, and J. C Dainty. "A low cost adaptive optics system using a membrane mirror", Optics Express, Vol. 6, No. 9, p. 175-185 (2000).